

1 Reflection of linear internal tides from realistic topography: The

2 Tasman continental slope

3 JODY M. KLYMAK, *

School of Earth and Ocean Sciences and Department of Physics and Astronomy, University of Victoria, Victoria, Canada

4 Harper L. Simmons and Dmitry Braznikov

University of Alaska Fairbanks, Fairbanks, Alaska, USA

Samuel Kelly

Large Lakes Observatory and Department of Physics, University of Minnesota Duluth, Duluth, Minnesota

Jennifer A. MacKinnon, Matthew H. Alford, and Robert Pinkel

Scripps Institution of Oceanography, University of California, San Diego, La Jolla, California

Jonathan D. Nash

College of Ocean and Atmospheric Science, Oregon State University, Corvallis, Oregon

*Corresponding author address: Jody Klymak, University of Victoria, Victoria, BC, Canada

E-mail: jklymak@uvic.ca

ABSTRACT

9 The reflection of a low-mode internal tide on the Tasman continental slope is investigated
10 using simulations of realistic and simplified topographies. The slope is super-critical to the
11 internal tide, which should predict a large fraction of energy reflected. However, the response
12 to the slope is complicated by a number of factors: the incoming beam is confined laterally;
13 it impacts the slope at an angle; there is a roughly cylindrical rise directly offshore of the
14 slope; and a leaky slope-mode wave is excited. These effects are isolated in simulations
15 that simplify the topography. In order to separate the incident from reflected signal, a
16 response without the reflector is subtracted from the total response to arrive at a reflected
17 signal. The real slope reflects approximately 65% of the mode-1 internal tide as mode-1,
18 less than two-dimensional linear calculations predict, due to the three-dimensional concavity
19 of the topography. It is also less than recent glider estimates, likely due to along-slope
20 inhomogeneity. The inhomogeneity of the response comes from the Tasman Rise which
21 diffracts the incoming tidal beam into two beams, one focused along-beam, and one diffracted
22 to the north. Along-slope inhomogeneity is enhanced by a partially trapped super-inertial
23 slope wave that propagates along the continental slope, locally removing energy from the
24 deep-water internal tide and re-radiating it into the deep water further north. This wave is
25 present even in a simplified straight-slope topography, its character can be predicted from
26 linear resonance theory, and it represents up to 30% of the local energy budget.

²⁷ 1. Introduction

²⁸ Energy is lost from the surface tide when it interacts with topography and, in the deep
²⁹ ocean, is largely redistributed as an internal tide. The fate of the internal tide is unclear, but
³⁰ depends on the dominant wavelengths that are forced. The internal tide response to topog-
³¹ raphy that is subcritical to the internal tide frequency is likely dominated by higher vertical
³² modes, and is thought to break via wave-wave interactions relatively close to the topography
³³ (i.e. Polzin 2009; St. Laurent and Garrett 2002). Steeper supercritical topography, while
³⁴ exhibiting significant local dissipation, tends to radiate a large fraction of the internal tide
³⁵ away from the topography as low-mode waves (i.e. at Hawaii; Klymak et al. 2006; Carter
³⁶ et al. 2008). Given that a significant fraction of the internal tide energy is generated at steep
³⁷ topography (Legg and Klymak 2008), and that the distribution of the mixing it eventually
³⁸ drives has impacts on understanding the distribution of ocean properties and the strength
³⁹ of the overturning circulation (i.e. Melet et al. 2013), it is desirable to understand where and
⁴⁰ how the radiated energy dissipates.

⁴¹ One candidate sink for the low-mode internal tide is scattering and dissipation from
⁴² continental slopes. These slopes are known to be hotspots of turbulent mixing from the few
⁴³ observational studies to date (Nash et al. 2007; Klymak et al. 2011; Martini et al. 2013).
⁴⁴ However, these studies have also demonstrated some of the difficulties in tracking internal tide
⁴⁵ energy on these slopes. Net internal-tide fluxes are relatively straight forward to measure,
⁴⁶ but ideally we would like to separate the incident and reflected fluxes if a parameterization of
⁴⁷ turbulence on the slope is to be made, since the incident fluxes are what drive the turbulence.
⁴⁸ The reflectivity of a continental slope is the ratio of the energy flux convergence divided by

49 the total incident flux:

$$R = \frac{F_{out}}{F_{in}}, \quad (1)$$

50 where F is depth-integrated for a two-dimensional budget or depth-line-integrated for a
51 three-dimensional one. Even simple two-dimensional linear models of reflection indicate
52 that determining the reflectivity will be challenging, with reflection co-efficients strongly
53 depending on the modal content and phases of the incident internal tides (Klymak et al.
54 2011) and the local surface tide (Kelly and Nash 2010). These linear models have been
55 used globally to estimate reflection co-efficients for the mode-1 tides on realistic continental
56 slope bathymetries, (Kelly et al. 2013b,a), but these calculations assume the incoming tide
57 is known, and that the topography is relatively homogenous over a distance similar to the
58 mode-1 horizontal wavelength.

59 Determining the incident flux, F_{in} , from field data, and even from a numerical model
60 with sufficient complexity, is not trivial. In two dimensions, or with simple plane-wave
61 geometries, it is straight forward to fit incident and reflected plane waves to recover the
62 desired reflection co-efficient. In the real ocean, even if tidal signals can be separated from
63 confounding influences, internal tides are often laterally inhomogeneous, and form lateral
64 “beams” (in x-y; Rainville et al. 2010) that make plane wave fits difficult from a finite array
65 of moorings; for instance a mooring array could be located more in the incoming beam than
66 in the reflected, leading to an exaggeration of the computed energy convergence. Plane-wave
67 fits to satellite altimetry tracks are promising, but will also suffer from a lack of fidelity if
68 the internal tides are inhomogeneous on the scale of the plane wave fits (Zhao and Alford
69 2009). In the model, high resolution temporal and spatial information makes it possible to

70 separate signals spectrally according to their direction of propagation (i.e. using a Hilbert
71 transform, Mercier et al. 2008), but this method works best if there are no boundaries and
72 the signals at the edges of the model domain can be tapered to reduce Gibbs ringing, neither
73 of which are applicable in the nearfield of a continental slope.

74 The region considered here is the Tasman continental slope, the focus of a concentrated
75 internal tide field experiment, TTIDE. As preliminary work, it has been sampled continu-
76 ously by gliders for a number of months in 2012 and 2013 (Johnston et al. 2015). The gliders
77 were piloted to form an antenna over which internal plane-wave fits were made. These ef-
78 forts show a standing wave pattern, with amplitudes and phases as one would expect for
79 internal waves incident on the slope from the southeast where internal tides are expected to
80 be generated from the Macquarie Ridge (figure 1a). The amplitudes of the interfering waves
81 were such that the reflectivity is predicted to be high on this slope, with estimates of 0.7 to
82 1.0 from the arrays (Johnston et al. 2015). The gliders also picked up a 100-km wavelength
83 wave propagating along slope towards the north, a finding we isolate and discuss below.

84 Here we run numerical simulations that are meant to represent a mode-1 internal M_2
85 tide incident on the Tasman Slope, east of Tasmania. The simulations are only forced
86 by the incident internal tide, and there is no barotropic forcing anywhere in the domain,
87 allowing the reflection signal to be isolated. After discussing the model setup (section 2),
88 we briefly consider the response this forcing has on the slope (section 3) and compute and
89 energy budget of the complete response. In order to separate the physics of the reflection,
90 we then simplify the geometry (section 4), both geometrically, and by removing parts of the
91 topography. This technique allows us to separate incident and reflected signals from the
92 total response without appeal to plane wave fits. We end with a discussion of the results

93 (section 5) where we note the applicability of two-dimensional reflection models and discuss
94 the leaky slope waves evident in the simulations. We conclude with a summary (section 6).

95 2. Model setup

96 a. Basics

97 The numerical model used here is the MITGCM (Marshall et al. 1997), visualized using
98 the Python scientific stack (Hunter 2007; van der Walt et al. 2011). The setup is very similar
99 to Buijsman et al. (2014), with the model run in hydrostatic mode, background (isotropic)
100 diffusivities and viscosities of $10^{-5} \text{ m}^2 \text{ s}^{-1}$, and enhanced diffusivity and viscosity in regions
101 of temporarily unstable stratification (Klymak and Legg 2010). A second-order flux-limiting
102 temperature advection scheme is used which results in some numerical dissipation and dif-
103 fusion. Sensitivity tests were run with weaker forcing, and the fraction of energy dissipated
104 in the model did not change, indicating that the dissipation highlighted below is dominated
105 by numerical dissipation due to the lack of lateral resolution (1 km) rather than explicit
106 viscosities. Dissipation is not the main focus of this paper, and finer resolutions have been
107 used for more focused efforts dealing with turbulence on the slope (in preparation).

108 Topography is from a data set that combines Smith and Sandwell (1997) and multibeam
109 data from Australian surveys (Whiteway 2009) (figure 1b). For this paper, we use a Cartesian
110 co-ordinate system centered at 44 S, 148 E, with y pointing 12 degrees east of geographic
111 north (magenta lines, figure 1). This co-ordinate system is close to cross-slope in the x-
112 direction, and is used for conceptual convenience. The simulations are run on a f-plane

₁₁₃ ($f = -10^{-4}$ s⁻¹).

₁₁₄ A 1-km lateral resolution is used along the continental slope (figure 2a, smallest inset
₁₁₅ green box). Resolution is expanded by 3.5% per grid cell beyond the 1km-resolution region,
₁₁₆ to a maximum of 5 km in the second largest inset box (figure 2a); this keeps the resolution
₁₁₇ over the Tasman Rise and the rest of the continental slope at least 5 km. Further out, the
₁₁₈ grid spacing is again increased at 3.5% per grid cell until a maximum grid cell size of 10 km
₁₁₉ is reached.

₁₂₀ Vertical resolution is approximately stretched so $dz \sim 1/N$, where $N^2(z) = -\frac{g}{\rho_0} \frac{d\rho}{dz}$ is the
₁₂₁ vertical stratification. 200 vertical grid cells are used for these simulations. The vertical
₁₂₂ stratification is from the World Ocean Atlas for the Tasman Sea just offshore of Tasmania
₁₂₃ (figure 1c Boyer et al. 2013), and is assumed to be initially laterally constant in the domain.
₁₂₄ This precludes any mesoscale effects, which are believed to be important in this area, and
₁₂₅ are the subject of future work.

₁₂₆ *b. Forcing*

₁₂₇ To simplify the generation problem we apply an analytical forcing to our model that
₁₂₈ is meant to represent a simplified version of the regional simulation pictured in figure 1a.
₁₂₉ This is composed of two line sources at approximately the location of the Macquarie Ridge
₁₃₀ (figure 2a). The initial conditions contain this wave field, and sponges in the southern and
₁₃₁ eastern boundaries are forced with it. The forcing is similar to that suggested by Rainville
₁₃₂ et al. (2010), except here our line source is digitized as a number of discrete point sources
₁₃₃ along the line, and their response in the domain summed. The mode-1 pressure anomaly is

¹³⁴ given by:

$$p'(x, y, t) = \sum_{i=1}^N p'_i = \sum_{i=1}^N \frac{a_i}{\sqrt{r_i}} \exp(j(|\mathbf{k}|r_i - \omega t)) \quad (2)$$

¹³⁵ where a_i is the amplitude of the i-th source, $r_i = \sqrt{(x - x_i)^2 + (y - y_i)^2}$ is the distance to
¹³⁶ the source, and $|\mathbf{k}|$ is the absolute value of the mode-1 wavenumber:

$$|\mathbf{k}| = \frac{(\omega^2 - f^2)^{1/2}}{c_e} \quad (3)$$

¹³⁷ where ω is the frequency of the tide, f is the Coriolis frequency, and c_e is the eigenspeed of
¹³⁸ the vertical mode equation:

$$\frac{d}{dz} \left(\frac{1}{N^2} \frac{d\psi}{dz} \right) + \frac{1}{c_e^2} \psi(z) = 0. \quad (4)$$

¹³⁹ Here $\psi(z)$ is the eigenfunction that sets the shape of the vertical mode, and the bound-
¹⁴⁰ ary conditions are $d\psi/dz = 0$ at $z = 0$ and $z = -H$, where H is the water depth. For
¹⁴¹ convenience, we normalize $\psi_m(z)$ so that

$$\int_{-H}^0 \psi_m(z) \psi_n(z) dz = \delta_{mn}. \quad (5)$$

¹⁴² Horizontal velocities can be linearly decomposed by these shapes, as can the pressure signal.
¹⁴³ To compute the wavefield, the horizontal velocity components are derived from the in-
¹⁴⁴ ternal wave consistency relations:

$$u(x, y, t) = \sum_{i=1}^N \frac{k_x \omega + j k_y f}{\omega^2 - f^2} \frac{p'_i}{\rho} \quad (6)$$

$$v(x, y, t) = \sum_{i=1}^N \frac{k_y \omega - j k_x f}{\omega^2 - f^2} \frac{p'_i}{\rho} \quad (7)$$

¹⁴⁵ where $k_x = |\mathbf{k}| \cos(\theta_i)$ and $k_y = |\mathbf{k}| \sin(\theta_i)$ are calculated from the angle to each element of
¹⁴⁶ the line sources $\theta_i = \arctan((y - y_i)/(x - x_i))$.

147 The resulting incoming wavefield (figure 2a) has a beam of energy flux that radiates
148 northwest, and is relatively tightly focused. The interference pattern creates a null to the
149 south and north, and a secondary beam that radiates due west. This schematic agrees with
150 more realistic regional tidal models (H. Simmons, in preparation), and the amplitude of the
151 beam was tuned to give approximately 2 kW m^{-1} incident at Tasmania. Note this is less
152 than estimates from altimetry and numerical simulations, and is purposely low to keep the
153 runs as “linear” as possible. The initial condition is applied uniformly through the domain,
154 regardless of bathymetry, so there are some start-up transients as the proper baroclinic flow
155 develops.

156 The sponge regions on the southern and eastern boundaries are forced with this forcing.
157 The northern and western boundaries are sponges where the velocity is slowly dropped to
158 zero and the stratification relaxed to the initial stratification (figure 2a, green rectangles).
159 Our main focus is the area from $y=0$ to 400 km, so the boundaries are sufficiently far that
160 small residual reflections do not affect the response.

161 The ideal response off the Tasman topography would be as a plane-wave reflection from
162 a wall at $x = 0$ km (i.e. Johnston et al. 2015). Here we have a relatively confined beam,
163 but we can make a start by considering the reflection the beam from a wall at $x = 0$ km for
164 $y > 0$ km (figure 2b,c) using the method of images with identical line sources mirrored about
165 the y-axis, and their phase shifted by 180 deg. The reflection pattern that sets up is not
166 entirely regular, but has some straight-forward features. The incoming beam impacts the
167 wall at approximately 30 deg. The horizontal wavelength of an M_2 internal tide is 178 km,
168 so the standing wave in the x-direction will have a wavelength $178/\cos(30) \approx 200$ km and
169 in the y-direction will have a wavelength of approximately 350 km. These spatial scales

170 are readily apparent in the analytical forcing despite the non-plane-wave character of the
171 idealized forcing (figure 2c). Note that the standing energy flux (figure 2b) has peaks and
172 nulls in absolute value, with the peaks having large flux to the north. The peaks are every
173 half cross-slope wavelength (i.e. 100 km). The nulls have weak southward energy flux (though
174 it is difficult to discern from the subsampled arrows in the plot).

175 3. Realistic model simulation

176 The response of the forcing in the most real bathymetry motivates the more idealized
177 experiments that follow. From the initial forcing (figure 3a), a complex wavefield develops
178 with clear scattering from the Tasman Rise, the shelf, and numerous small inhomogeneities
179 on the sea floor (figure 3b–d). Looking along slope, the phase of the velocity signal can
180 be seen changing approximately every 200 km, and it changes approximately every 100 km
181 offshelf similar to what we expect from an oblique standing wave (compare figure 3h to
182 figure 2b). However the pattern is complicated, not lining up in the north-south direction
183 and inhomogeneities in the energy that are not accounted for by a simple two-wave model.

184 A time-averaged energy balance is performed online in the model using the terms outlined
185 in Kang and Fringer (2012); Kang (2011). The energy balance vertically integrated can be
186 schematized as:

$$dE_{bc}/dt = -\nabla_H \cdot \mathbf{F}_{bc} + \text{Conversion} - \text{Dissipation}. \quad (8)$$

187 where E_{bc} is the depth-integrated baroclinic energy density, $-\nabla_H \cdot \mathbf{F}_{bc}$ is the depth integrated
188 baroclinic energy flux convergence, including both the pressure work term and the non-linear

advection of energy (which is small in our runs). All quantities are averaged over an M_2 tidal period. “Conversion” is a complex term representing transfer from barotropic motions to baroclinic (Kang 2011, eq. 5.102) and includes the barotropic heaving of the water column, the density anomaly, and a non-linear horizontal advection term. These non-linear terms can be non-trivial in real bathymetry (Buijsman et al. 2014). The conversion term is positive if the barotropic tide loses energy and the baroclinic tide gains energy. “Dissipation” is computed here as the residual, and includes dissipation due to explicit viscosity, numerical dissipation, and bottom drag.

Of note in the energy calculation is that the largest local term in the energy budget is an alternating pattern of barotropic-baroclinic conversion at the shelf break, mostly balanced by baroclinic flux convergences and divergences (figure 4). The importance of the barotropic-baroclinic term can also be seen by considering the x-integral of the energy budget from $x = -50$ km to $+100$ km (figure 5). Recall that the simulations have no barotropic forcing. This coupling is driven by the interaction of the internal tide and the shelf corner at $y = 0$, and takes the form of a leaky super-inertial slope wave (see section 5).

The time series of the energy terms integrated in the volume bounded by $x = 0$ to 80 km and $y = 0$ to 400 km demonstrates that the barotropic-to-baroclinic term is relatively small when averaged, with a small loss of energy from the baroclinic tide to the barotropic in the integral region (figure 5b). The model is largely in a steady state by tidal cycle 15, with some residual oscillations in dE/dt and the flux convergence. The oscillations were not explicitly examined, but likely result from imperfect sponges. The large-scale baroclinic energy changes do not change the dissipation residual very much, which is relatively constant after 5 tidal cycles. To put the 50 MW of dissipation into context, the initial energy that comes in the

212 east and south sides of this analysis box in the initial conditions is 315 MW, so the model
213 is dissipating about 17% of the incoming energy. However, note that the dissipation is not
214 the focus of these model runs nor of this paper. The forcing here is approximately a factor
215 3 lower than the real forcing, so its likely the fraction of dissipation at this site is higher if
216 real forcing is used.

217 The majority of the energy budget is in the first vertical mode (figure 5c). Net fluxes
218 in the region directly offshore of the shelf break ($0 < x < 80$ km, and $0 < y < 400$ km)
219 are composed of substantial mode-1 energy converging on the slope (95 MW net), and some
220 reflected energy escaping in higher modes (28.3 MW, mostly in modes 2–4). The 95 MW net
221 flux is made up of the incoming and reflected mode-1 energy, and separating those terms is
222 the subject of the next section. There is some incoming higher-mode energy as well due to
223 scattering from the Tasman Rise, but as we will also show below, this is minor. The spatial
224 pattern (not shown) of the mode conversion at the continental slope indicates hot-spots for
225 conversion. Modes 2 and 4 have a hotspot of conversion near $y = 250$ km, and mode 3 at
226 $y = 325$ km.

227 4. Simplified geometries

228 To help tease apart the effects of the Tasman Rise and the non-uniform slope, we carry
229 out a few simplified experiments (figure 6; figure 7). The REAL case is the one discussed
230 above (figure 7f). The NO TOPO case has no topography at all (figure 7a), just the beam
231 being forced at the south and east boundaries and (mostly) absorbed at the west and north.
232 RISE was run with the real bathymetry west of $x = 70$ km (figure 7e). Three idealized ge-

233 geometries simplify the physics even more: the SHELF case has a supercritical two-dimensional
 234 continental slope running north from $y = 0$ km (figure 7d). ROUND RISE is a 1700-m tall
 235 cylinder-shaped bump with radius of 50 km centered at approximately the same location as
 236 the Tasman Rise, with no shelf to the west (figure 7b). The simplified slope and the rise are
 237 both used in the SHELF/RISE case (figure 7c).

238 *a. Shelf-only configuration*

239 The simplest topography is the SHELF configuration (figure 7d). Here we have a response
 240 that is quite similar to the analytical response calculated above (figure 2b). The only differ-
 241 ence between these two cases is the narrow shelf west of $x = 0$ km and the continental slope
 242 instead of a wall. The interference pattern between the incoming wave and the reflected
 243 wave is clear in this plot, with the same characteristic length scales as above, and a slight
 244 bending of the response due to the radial spreading of the beam.

245 The goal of this paper is to determine the amount of reflectivity of the continental slope.
 246 This is a hard number to determine in a complicated geometry, and naturally depends on
 247 the region of integration. For the SHELF configuration the situation is relatively simple, and
 248 we use it to illustrate the numerical technique used below. The signal in the full simulation
 249 is assumed to consist of an “incoming” signal and a reflected signal, so we can decompose
 250 the east-west velocity amplitude of the first vertical mode (for example) as:

$$u_1^t(x, y) = u_1^i + u_1^r \quad (9)$$

$$v_1^t(x, y) = v_1^i + v_1^r \quad (10)$$

$$p_1^t(x, y) = p_1^i + p_1^r \quad (11)$$

251 where u_1^t is the (total) complex amplitude of the M_2 , mode-1 east-west velocity of the
 252 simulation with the reflection, u_1^i of the incoming signal, and u_1^r of the reflected signal. We
 253 assume for this example that the incoming signal u_1^i is given by the NO TOPO simulation,
 254 and u_1^t is from the SHELF simulation. The reflected signal u_1^r is simply the difference of these
 255 two. This method has been used by Hall et al. (2013) for a two dimensional flow. Here it is
 256 an absolute necessity because of the complicated three-dimensional topography.

257 In order to compute an energy budget, the energy fluxes are calculated from the decom-
 258 posed signals as:

$$F_{x1}^t = u_1^t p_1^t \quad (12)$$

$$= \underbrace{u_1^i p_1^i}_{\text{Incoming}} + \underbrace{u_1^r p_1^r}_{\text{Reflected}} + \underbrace{u_1^i p_1^r + u_1^r p_1^i}_{\text{Cross Terms}} \quad (13)$$

$$F_{y1}^t = v_1^t p_1^t \quad (14)$$

$$= \underbrace{v_1^i p_1^i}_{\text{Incoming}} + \underbrace{v_1^r p_1^r}_{\text{Reflected}} + \underbrace{v_1^i p_1^r + v_1^r p_1^i}_{\text{Cross Terms}} \quad (15)$$

259 The cross terms are not negligible for any realistic forcing, and indeed give rise to the
 260 interference patterns seen above (Nash et al. 2004; Martini et al. 2007).

261 The “total” response (figure 8d) consists of the incoming response (figure 8a), and the
 262 “reflected” signal (figure 8b), and substantial cross-terms (figure 8c). The cross terms are
 263 mostly perpendicular to the direction of reflection (i.e. parallel to the slope) and alternately
 264 flux energy to the north and south every half cross-slope wavelength. Combined, these three
 265 components give the “total” flux with net fluxes to the north in alternating peaks every full
 266 offslope wavelength.

267 The reflected response (figure 8b) shows approximately what we would expect with energy
 268 being radiated to the north-east. There is some concentration of this energy at $y \approx 75\text{km}$,

269 and $y \approx 225\text{km}$ because of coupling with a partially trapped slope wave. This coupling
270 causes a redistribution of the reflected energy, focusing it approximately every along-slope
271 wavelength of the slope wave (we show in section 5 that this wavelength changes as the slope
272 geometry changes).

273 Performing this analysis for the lowest 10 modes, we arrive at an energy budget for the
274 slope in the green box in the figures ($0 < y < 400\text{ km}$, and $x < 80\text{ km}$; figure 8, inset
275 budgets). Note that we assume the flux through $x = 0$ is zero. With this calculation, we see
276 that 408 MW is incident on the slope in mode-1. There is also a net flux of 50 MW into this
277 region from the cross terms. This is a redistribution of energy from north of our box into
278 the box. There is a net convergence of this cross-term energy because there is dissipation in
279 the box; in a purely inviscid solution this term should balance to zero over a closed box. If
280 we extend the integration further north, the cross-term flux drops to zero.

281 Most of the incoming energy reflects back out of the box (figure 8b), with the bulk
282 remaining in mode 1, and some scattering to higher modes. This scattered energy radiates
283 to the north east (not shown). The mode-1 reflection is affected by the slope wave that
284 transfers energy to and from the barotropic tide along the slope, resulting in nulls and peaks
285 in the mode-1 reflection.

286 *b. Tasman Rise and Simplified Shelf*

287 The Tasman Rise has a profound effect on the energy that impacts the continental slope
288 (figure 7e and f). The incoming beam is almost 500 km wide at $x = 0$ if there is no
289 Tasman Rise, but breaks into three narrower beams when there is a Tasman Rise (figure 7e).

290 Upstream of the rise, the effect is somewhat less energy propagating westward, with an
291 interference pattern towards the east indicating some back reflection.

292 This pattern can be explained in terms of diffraction of the internal tide beam from a
293 deep obstacle (i.e. Johnston and Merrifield 2003). There is a down-wave concentration of
294 energy along the seamount's axis, a null, and sidelobes to the north and south. In this case,
295 the incident beam is of comparable size to the obstacle, leading to an asymmetry, and a
296 stronger lobe to the north than south.

297 Most of the response due to the Tasman Rise can be modeled simply as a cylindrical
298 obstacle in the beam (figure 7b and c). Here our obstacle is 1800 m high in 5000 m of
299 water, and has a radius of 50 km (figure 6). This captures most of the features of the actual
300 Tasman Rise, despite not having a shallow spire in the center and being slightly smaller than
301 the real Rise. The differences make the simplified response have weaker nulls and the whole
302 response is directed a bit further north than the real Rise. Adding the shelf (figure 7c) yields
303 a response that bears substantial similarity to the REAL forcing case.

304 Decomposing into an incoming and reflected signal (figure 9) demonstrates the effect of
305 the Tasman Rise on the response. Less energy is incident on the control volume, largely
306 because the diffraction redirects some of that energy to the north of $y = 400$ km. There is a
307 strong reflection of energy where the main diffraction lobe reflects from the slope (figure 9b),
308 and a smaller maximum just to the north ($y = 250$ km) due to the along-slope wave that
309 is strummed. There is a reflection further north where the northern lobe of the diffraction
310 pattern reflects.

311 The incoming energy has some more high-mode content due to scattering at the cylindri-
312 cal rise (figure 9a), though it is still 95% mode-1. The reflection is almost 80% mode-1, with

313 some scattering to higher modes. The net flux shows approximately 15% of the incoming
314 energy is dissipated at the shelf.

315 *c. Real Case*

316 The REAL forcing is similar, if more complex (figure 10). The simulation using the
317 bathymetry in the RISE ONLY case (figure 7e) is used as the “Incoming” energy flux, and
318 the REAL (figure 7f) case is the “Total”. Compared to the cylindrical rise, the real Tasman
319 Rise creates a sharper diffraction pattern, and more back reflection. However, the REAL
320 simulation has many of the same features as the SHELF/RISE simulation (figure 7c).

321 Slightly less incoming energy passes into the control volume (figure 10a) because the
322 diffraction by the real Tasman Rise is sharper than the cylindrical rise. As for the cylindrical
323 rise case, there is some incoming higher mode energy due to forward scattering, though again
324 over 95% is mode-1. Reflection is concentrated near $y = 125$ km and $y = 450$ km, associated
325 with the diffraction nodes, with about 85% in mode 1 (figure 10b). Dissipation is less than
326 25% of the incoming energy (figure 10d).

327 **5. Discussion**

328 *a. Estimating reflection co-efficients*

329 A major goal of this effort is estimating the fraction of incoming tide that is reflected by
330 the Tasman continental slope to come up with a reflectivity co-efficient. Here we discriminate
331 between the mode-1 reflection, $R_1 = F_{ref,1}/F_{in,1}$, and the total reflection into all the modes,

332 $R_T = F_{ref}/F_{in}$. Evaluating these co-efficients is less straightforward than it may sound
333 because it is difficult to separate the incoming from reflected signal in complicated geometry,
334 even in a fully resolved numerical model, let alone in observations. Above, we used an
335 integrated measure, comparing the incoming flux from a model with no continental slope to
336 one with a continental slope and integrating the fluxes over a control volume from $y = 0$ to
337 400 km. This control volume was an arbitrary choice, but yielded reflectivities of mode-1
338 internal tide $R_1 = 0.65$ and the total internal tide of $R_T = 0.76$ (figure 10).

339 The TTIDE field effort deployed a three-point mooring array to quantify the wave field
340 offshore of the continental slope. Determining reflectivity from such a mooring array is sig-
341 nificantly complicated by three-dimensionality and along slope variability. From the mooring
342 array in figure 10, the reflectivity is $R_1 = 0.6/1.3 = 0.46$, a significant under-estimate. The
343 reason for this should be relatively clear from looking at figure 10a,b; the mooring array
344 nicely captures the northward diffracted ray, but catches some of the reflected pattern from
345 the main beam to the south. There are significant interferences in the reflected patterns
346 (figure 10b) because the reflected pattern is a complicated superposition of the cylindrically
347 spreading reflections along the slope.

348 Determining the reflectivity as a function of along-slope direction y is difficult. A simple
349 one-dimensional comparison of onslope and offslope fluxes does not yield useful results be-
350 cause the reflection from any given point on the slope radiates cylindrically, so it is necessary
351 to integrate over volumes. Here we take the same approach as used in the previous section
352 (i.e. figure 10), but integrate over smaller control volumes (80 km in y , and between 0 and
353 80 km in x) to see the reflectivity as a function of y (figure 11a,b). The incoming flux every
354 80 km shows the diffracted beam pattern with a maximum net incoming flux at $y = 120$ km

355 (figure 11a, red line) and a secondary peak to the north at about 440 km. The net reflectivity
356 from these boxes ranges from 0.8 to a low of almost zero at $y = 280$ km where the slope is less
357 steep (figure 11b, solid blue line). Note an uncertainty in the flux decomposition associated
358 with the flux in the cross terms (figure 11a, purple line). This term does not balance to zero,
359 and forms a significant part of the energy budget over such small control volumes. It cannot
360 be uniquely decomposed into either the incoming or reflected energy terms, so remains as
361 an uncertainty.

362 In two-dimensions, the fraction of the tide reflected into mode 1 (and higher) can be
363 predicted from linear theory using the method described by Kelly et al. (2013a) of matching
364 Laplacian tidal solutions at discrete steps on a discretized topography. If the tide is obliquely
365 incident on the slope, there can be substantial differences in the reflected tide (Kelly et al.
366 2013b). If we run these solutions for the Tasman Slope with an incident angle of 30 degrees,
367 the reflectivity into mode-1, R_1 is similar to the numerical simulation (figure 11b, thick black
368 line). The predicted reflectivity is greater for most of the ridge, but the null at $y = 250$ km
369 is captured.

370 The REAL simulation has a mode-1 reflectivity of $R_1 = 0.65$. A naive average of the
371 reflectivity from the linear model between $y = 0$ and 400 km yields $\langle R_1 \rangle = 0.71$. However,
372 that does not take into account the varying strength of the incoming diffracted beam, which
373 is stronger where the reflectivity is higher. Weighting by the incoming beam strength, then
374 the reflectivity averages $\langle R_1 \rangle_{beam} = 0.8$, and is substantially larger than in the numerical
375 simulations.

376 An attempt has been made to estimate reflectivity from this site from autonomous gliders
377 surveys (Johnston et al. 2015). First, the gliders saw a substantial concentration of energy

378 shoreward of the Tasman Rise. This is a feature of the model, and clearly explained by the
379 diffraction of energy by the Tasman Rise (figure 10).

380 For the region in the lee of the Tasman Rise, Johnston et al. (2015) estimate a reflectivity
381 of the mode-1 internal tide of between 0.8 to 1.0 by fitting plane waves to the velocity and
382 displacement amplitudes and phases. If we confine our incoming versus outgoing energy
383 budget to the region $80 \text{ km} < y < 200 \text{ km}$, representative of their *Spray 56* deployment, we
384 calculate a reflectivity of 0.7, which is lower than their lowest estimate of 0.8, and much lower
385 than their high estimate of 1.0. A second deployment, *Spray 55*, covered more of the slope
386 (up to $y = 300 \text{ km}$). In this domain, they estimate a reflectivity of 0.6. This is in agreement
387 with the numerical simulation, which achieves the same result from $0 \text{ km} < y < 300 \text{ km}$.

388 The directions of wave propagation fit from the glider data is not in agreement with the
389 model. The fits to the *Spray 55* data show incoming energy at between 125 and 145 degrees,
390 which is similar to the model. However the reflection is slightly south of due east (0 to
391 -30 degrees geographic), whereas the numerical model is definitely to the northeast far from
392 shore. An explanation is evident from close inspection of figure 10b between the Tasman
393 Rise and the continental slope, where the glider spent the most time. At this location the off-
394 shore energy flux is almost exactly in the x-direction, (-12 degrees geographic), in agreement
395 with the glider observations.

396 Finally, one of the gliders (*Spray 56*) picked out a northward propagating disturbance
397 along the continental slope with wavelength of 100 km. This wavelength matches the wave-
398 length of the slope wave seen in the real simulations (figure 4a,b). Interestingly, they only
399 pick this wavelength out in vertical displacement data, not in velocity.

400 b. Slope wave importance and dynamics

401 The structure of the barotropic-to-baroclinic conversion on the slope is an intriguing fea-
402 ture of these simulations, and appears in regional simulations (Simmons, in prep) and the
403 glider data (Johnston et al. 2015). Here, it shows up most clearly in the SHELF simulations
404 because of the simplified bathymetry. However, it is also clear in the REAL simulation (fig-
405 ure 4a). This slope wave redistributes energy in the reflected baroclinic response (figure 8),
406 taking a relatively homogenous incoming energy source and focusing the reflection every 200
407 km or so along slope.

408 This wave is a slope mode that is strummed by the incident internal tide at the “corner” of
409 the topography ($x = 0, y = 0$); a long slope without the corner does not excite this wave, nor
410 does an internal tide coming directly from the east and hitting the topography at a normal
411 angle. The along-slope wavelength is independent of the incident along-slope wavelength
412 in the open water (tested by changing the angle of the incident tide; not shown), and is a
413 robust feature of the slope shape. A sensitivity experiment that varied the continental slope
414 widths demonstrates that narrower slopes strum longer along-slope waves (figure 12).

415 These waves are super-inertial and are an example of partially trapped slope waves (Dale
416 and Sherwin 1996; Dale et al. 2001). We compare the wavelength of the slope waves (fig-
417 ure 13, thick lines) to the empirical modes predicted from linear theory (Dale et al. 2001).
418 The procedure solves for the response of the flow in the coastal bathymetry due to forcing
419 with varying along-slope wavelengths. Resonant along-slope wavelengths lead to a much
420 stronger response (Appendix and figure 13, thin lines). The along-slope wavelength of the
421 resonant modes in the linear calculation agree quite well with the wavelengths of the fully

422 non-linear solutions. Narrower continental slopes yield longer along-slope wavelengths, and
423 the spatial modes that correspond to the peaks are similar to deep-ocean mode-1 off the
424 slope.

425 The slope wave is an important term in the local energy budget when compared the
426 incoming and reflected energy fluxes (figure 14). The incoming energy peaks at 1.2 kW/m,
427 and the reflected energy is of a similar magnitude but with oscillations at twice the wave-
428 length of the slope wave. The integrated barotropic-baroclinic conversion is as high as 0.4
429 kW/m-coastline, and leads to 0.4 kW/m peak-to-peak oscillation in the reflected energy (its
430 not 0.8 kW/m peak-to-peak because the reflected energy spreads spherically by $x = 40$ km,
431 where the reflected flux is evaluated, figure 8). This turns even a relatively straight slope
432 into a series of internal tide absorbers and radiators, leading to 100-km scale inhomogeneity
433 in the reflected internal tide.

434 6. Summary

435 A mode-1 internal tide was launched at a variety of topographies representing the Tasmanian
436 continental slope. The goal was to determine the “reflectivity” of this slope, in terms of
437 the modal content of the reflected energy and the local dissipation. The latter is somewhat
438 suspect in this model because of crude lateral resolution, but the REAL simulation indicated
439 that 21% of the incoming energy was dissipated, and 65% was reflected as mode-1 energy.
440 The incoming internal tide flux used here was weak compared to the flux modeled and in-
441 ferred from altimetry in the Tasman Sea, so we expect the dissipation in more realistically
442 forced models to increase.

443 Despite a simple incoming internal tide that is linear, semi-diurnal, and mode-1, we have

444 found a rich and complex response when the remote wave impacts the topography. The

445 response can be characterized as follows:

446 • diffraction of the beam by the Tasman Rise,

447 • oblique reflection from the continental slope,

448 • and a leaky slope wave response that redistributes reflected internal energy along-slope.

449 Of these, perhaps only the second effect was expected before carrying out the simulations.

450 However, as we saw above, even the reflection problem is significantly complicated in the

451 presence of three-dimensionality.

452 Diffraction around underwater topography should have been expected, however, the rel-

453 ative depth of the Tasman Rise makes it surprising that the effect is so strong. The fact that

454 the lateral width of the Rise is close to the wavelength of the incoming internal tide makes

455 predicting the diffraction pattern difficult. Baines (2007) considers generation of internal

456 tides at seamounts, but does not deal with scattering and diffraction. The problem is similar

457 to electromagnetic waves passing through a wire, but a linear response for that problem is

458 not trivial to compute (i.e. Bonod et al. 2005), and does not have a confined vertical mode

459 structure as we find in the internal wave problem.

460 The excitation of slope waves has been explored by Dale et al. (2001). It has an important

461 effect on the redistribution of energy along slope. The redistribution affects where high

462 dissipation is found in the model (figure 4), and adds more inhomogeneity to the reflected

463 internal tide.

464 The complexity grows if other real-world influences are to be accounted for. The East
465 Australian Current flows along this slope, varying the stratification in the horizontal, provides
466 lateral shears that can distort the internal tide response, and carrying eddies that can add
467 a strong time dependence to these effects. Even in two dimensions, the strength of the
468 internal tide reflection can be significantly impacted by the phase of the incoming tide with
469 other baroclinic modes Klymak et al. (2011) or the barotropic (Kelly and Nash 2010). The
470 simulations here exclude the local barotropic tide, so this would certainly complicate the
471 reflected response. Finally, the internal tide used here was monotonic, whereas the real tide
472 will also have other frequencies, most notably subinertial diurnal frequencies that will have
473 trapped wave responses (personal communication, R. Musgrave).

474 Regardless, it is useful to have studied the “simplest” response we could in this system
475 to tease apart the dominant physics. This response is complex, and it should be clear that
476 solely observational efforts to balance a reflection budget are going to be a challenge. Merging
477 simulations and observations is a likely way forward in understanding the wave field in this
478 complex slope region.

479 With respect to the reflection problem, the modeled slope has a relatively high reflection
480 back into the open ocean, with as much as 65% of the incoming energy being reflected as
481 mode-1. Its possible that higher resolution runs will be more dissipative, and that stronger
482 forcing will lead to a higher fraction of dissipation. However, these simulations, and the
483 results from the rest of the experiment to date (i.e. Johnston et al. 2015) indicate that bulk
484 of the energy from the Macquarie Ridge must dissipate elsewhere.

485 *Acknowledgments.*

486 Our thanks to conversations with Andy Dale on leaky slope waves and Qiang Li for
487 sharing his linear code for the Lindzen-Kuo method. J. Klymak was supported by the
488 Canadian National Science Engineering Research Council Discovery Grant 327920-2006, and
489 by computer time from the US Office of Naval Research, T. Palusziewicz, program officer.
490 H. Simmons and D. Brazhnikov were supported by NSF OCE 1130048. J. MacKinnon, and
491 R. Pinkel were supported by award NSF OCE 1129763. M. Alford was supported by NSF
492 OCE 1129246. A website for this paper with analysis scripts, intermediate data files, and
493 model setups is at <http://web.uvic.ca/~jklymak/ttide15>.

APPENDIX

Appendix Slope-wave calculation

497 The slope wave calculation follows the calculation made by Dale et al. (2001), where

498 there are more details. The linear equation for the pressure perturbations are assumed to

499 have form $P = p(x, z) \exp^{i(k_y y - \omega t)}$, where k_y is the along-slope wavenumber.

$$(f^2 - \omega^2) \frac{\partial}{\partial z} \left(\frac{\partial p / \partial z}{N^2 - \omega^2} \right) + \frac{\partial^2 p}{\partial x^2} - k_y^2 p = 0 \quad (\text{A1})$$

500 Subject to boundary conditions at the surface of $\partial p / \partial z = 0$ and at the sea floor of

$$\left(\frac{\omega^2 - f^2}{N^2 - \omega^2} \right) \frac{\partial p}{\partial z} = \frac{\partial h}{\partial x} \left(\frac{\partial p}{\partial x} - \frac{f k_y}{\omega} p \right) \quad (\text{A2})$$

501 The coast is assumed to be a wall, and the open ocean to consist of waves radiating away

502 from the slope, or if k_x , the cross-slope wavenumber, is imaginary, disturbances that decay

503 away from the slope.

504 The above are discretized on a domain that is 260 km wide into 261 grid cells in x ,

505 and onto a sigma-co-ordinate with 192 vertical levels. The hyperbolic method of solution

506 due to Lindzen and Kuo (1969) was used to solve on this domain for p for $\omega = 1.4f$,

507 $f = 10^{-4} \text{s}^{-1}$, and for a sweep of k_y . Under an arbitrary forcing certain values of k_y resonate

508 and lead to stronger amplitude responses in p corresponding to spatial modes of the system.

509 The numerical method is sensitive to the stratification, so we used a fit exponential of

510 $N^2(z) = 2 \times 10^{-5} \text{s}^{-2} e^{z/(1000 \text{ m})}$ (where z is negative downwards). The scan was taken over

511 300 wavelengths equally spaced between 30 and 180 km.

512 The resulting spatial modes are similar to those in Dale et al. (2001) (figure 15). There
513 is a peak of amplitude on the shelf, and then a second peak on the slope. As the slope gets
514 more narrow, the peak on the slope becomes broader. These shapes are the lowest modes.

515 The general code to solve this is at <https://github.com/jklymak/LindzenKuo>. The
516 code used for this paper is at <http://web.uvic.ca/~jklymak/ttide15/>.

REFERENCES

- 519 Baines, P. G., 2007: Internal tide generation by seamounts. *Deep Sea Res. I*, **54** (9), 1486 –
 520 1508, doi:10.1016/j.dsr.2007.05.009.
- 521 Bonod, N., E. Popov, and M. Nevière, 2005: Differential theory of diffraction by finite
 522 cylindrical objects. *JOSA A*, **22** (3), 481–490, doi:10.1364/JOSAA.22.000481.
- 523 Boyer, T., et al., 2013: *World Ocean Database 2013*. NOAA Atlas NESDIS 72, doi:10.7289/
 524 V5NZ85MT.
- 525 Buijsman, M. C., et al., 2014: Three-dimensional double-ridge internal tide resonance in
 526 Luzon Strait. *J. Phys. Oceanogr.*, **44** (3), 850–869, doi:10.1175/JPO-D-13-024.1.
- 527 Carter, G., et al., 2008: Energetics of M 2 Barotropic-to-Baroclinic Tidal Conversion at the
 528 Hawaiian Islands. *Journal of Physical Oceanography*, **38** (10), 2205–2223, doi:10.1175/
 529 2008JPO3860.1.
- 530 Dale, A. C., J. M. Huthnance, and T. J. Sherwin, 2001: Coastal-trapped waves and
 531 tides at near-inertial frequencies. *J. Phys. Oceanogr.*, **31** (10), 2958–2970, doi:10.1175/
 532 1520-0485(2001)031<2958:CTWATA>2.0.CO;2.
- 533 Dale, A. C. and T. J. Sherwin, 1996: The extension of baroclinic coastal-trapped wave
 534 theory to superinertial frequencies. *J. Phys. Oceanogr.*, **26** (11), 2305–2315, doi:10.1175/
 535 1520-0485(1996)026<2305:TEOBCT>2.0.CO;2.

- 536 Hall, R. A., J. M. Huthnance, and R. G. Williams, 2013: Internal wave reflection on shelf
537 slopes with depth-varying stratification. *J. Phys. Oceanogr.*, **43** (2), 248–258, doi:10.1175/
538 JPO-D-11-0192.1.
- 539 Hunter, J. D., 2007: Matplotlib: A 2D graphics environment. *Comput. Sci. Eng.*, **9** (3),
540 90–95, doi:10.1109/MCSE.2007.55.
- 541 Johnston, T. M. S., D. L. Rudnick, and S. M. Kelly, 2015: Standing internal tides in the Tas-
542 man Sea observed by gliders. *J. Phys. Oceanogr.*, **45** (11), doi:10.1175/JPO-D-15-0038.1.
- 543 Johnston, T. S. and M. A. Merrifield, 2003: Internal tide scattering at seamounts, ridges,
544 and islands. *J. Geophys. Res.*, **108** (C6), 3180, doi:10.1029/2002JC01528.
- 545 Kang, D., 2011: Barotropic and baroclinic tidal energy. Ph.D. thesis, Stanford University.
- 546 Kang, D. and O. Fringer, 2012: Energetics of barotropic and baroclinic tides in the Monterey
547 Bay area. *J. Phys. Oceanogr.*, **42** (2), 272–290, doi:10.1175/JPO-D-11-039.1.
- 548 Kelly, S. and J. Nash, 2010: Internal-tide generation and destruction by shoaling internal
549 tides. *Geophys. Res. Lett.*, **37**, L23 611, doi:10.1029/2010GL045598.
- 550 Kelly, S. M., N. L. Jones, and J. D. Nash, 2013a: A coupled model for Laplace's tidal
551 equations in a fluid with one horizontal dimension and variable depth. *J. Phys. Oceanogr.*,
552 doi:10.1175/JPO-D-12-0147.1.
- 553 Kelly, S. M., N. L. Jones, J. D. Nash, and A. F. Waterhouse, 2013b: The geography of
554 semidiurnal mode-1 internal-tide energy loss. *Geophys. Res. Lett.*, doi:10.1002/grl.50872.

- 555 Klymak, J., M. Alford, R. Pinkel, R. Lien, Y. Yang, and T. Tang, 2011: The breaking and
556 scattering of the internal tide on a continental slope. *J. Phys. Oceanogr.*, **41**, 926–945,
557 doi:10.1175/2010JPO4500.1.
- 558 Klymak, J. M. and S. M. Legg, 2010: A simple mixing scheme for models that resolve
559 breaking internal waves. *Ocean Modell.*, **33** (3-4), 224 – 234, doi:10.1016/j.ocemod.2010.
560 02.005.
- 561 Klymak, J. M., et al., 2006: An estimate of tidal energy lost to turbulence at the Hawaiian
562 Ridge. *J. Phys. Oceanogr.*, **36**, 1148–1164, doi:10.1175/JPO2885.1.
- 563 Legg, S. and J. M. Klymak, 2008: Internal hydraulic jumps and overturning generated by
564 tidal flow over a tall steep ridge. *J. Phys. Oceanogr.*, **38** (9), 1949–1964, doi:10.1175/
565 2008JPO3777.1.
- 566 Lindzen, R. and H.-L. Kuo, 1969: A reliable method for the numerical integration of a large
567 class of ordinary and partial differential equations. *Mon. Wea. Rev.*, **97** (10), 732–734,
568 doi:10.1175/1520-0493(1969)097<0732:ARMFTN>2.3.CO;2.
- 569 Marshall, J., A. Adcroft, C. Hill, L. Perelman, and C. Heisey, 1997: A finite-volume, incom-
570 pressible Navier-Stokes model for studies of the ocean on parallel computers. *J. Geophys.
571 Res.*, **102** (C3), 5753–5766, doi:10.1029/96JC02775.
- 572 Martini, K., M. Alford, J. Nash, E. Kunze, and M. Merrifield, 2007: Diagnosing a partly
573 standing internal wave in Mamala Bay, Oahu. *Geophys. Res. Lett.*, **34** (17), L17604,
574 doi:10.1029/2007GL029749.

- 575 Martini, K. I., M. H. Alford, E. Kunze, S. M. Kelly, and J. D. Nash, 2013: Internal bores and
576 breaking internal tides on the Oregon continental slope. *J. Phys. Oceanogr.*, **43**, 120–139,
577 doi:10.1175/JPO-D-12-030.1.
- 578 Melet, A., R. Hallberg, S. Legg, and K. Polzin, 2013: Sensitivity of the ocean state to the
579 vertical distribution of internal-tide-driven mixing. *J. Phys. Oceanogr.*, **43** (3), 602–615,
580 doi:10.1175/JPO-D-12-055.1.
- 581 Mercier, M. J., N. B. Garnier, and T. Dauxois, 2008: Reflection and diffraction of internal
582 waves analyzed with the Hilbert transform. *Phys. Fluids*, **20** (8), 086 601, doi:10.1063/1.
583 2963136.
- 584 Nash, J., M. Alford, E. Kunze, K. Martini, and S. Kelley, 2007: Hotspots of deep
585 ocean mixing on the Oregon continental slope. *Geophys. Res. Lett.*, **34**, L01 605,
586 doi:10.1029/2006GL028 170.
- 587 Nash, J. D., E. Kunze, J. M. Toole, and R. W. Schmitt, 2004: Internal tide reflection and
588 turbulent mixing on the Continental Slope. *J. Phys. Oceanogr.*, 1117–1134, doi:10.1175/
589 1520-0485(2004)034<1117:ITRATM>2.0.CO;2.
- 590 Polzin, K. L., 2009: An abyssal recipe. *Ocean Modelling*, **30** (4), 298–309, doi:10.1016/j.
591 ocemod.2009.07.007.
- 592 Rainville, L., T. Johnston, G. S. Carter, M. A. Merrifield, R. Pinkel, P. F. Worcester, and
593 B. D. Dushaw, 2010: Interference pattern and propagation of the M_2 internal tide south
594 of the Hawaiian Ridge. *J. Phys. Oceanogr.*, **40** (2), doi:10.1175/2009JPO4256.1.

- 595 Smith, W. and D. Sandwell, 1997: Global sea floor topography from satellite altimetry and
596 ship depth soundings. *Science*, **277** (5334), 1956, doi:10.1126/science.277.5334.1956.
- 597 St. Laurent, L. and C. Garrett, 2002: The role of internal tides in mixing the deep ocean. *J.*
598 *Phys. Oceanogr.*, **32**, 2882–2899, doi:10.1175/1520-0485(2002)032<2882:TROITI>2.0.CO;
599 2.
- 600 van der Walt, S., S. C. Colbert, and G. Varoquaux, 2011: The NumPy array: A structure
601 for efficient numerical computation. *Comput. Sci. Eng.*, **13** (2), 22–30, doi:10.1109/mcse.
602 2011.37.
- 603 Whiteway, T., 2009: Australian bathymetry and topography grid, june 2009. scale 1:5000000.
604 Tech. rep., Geoscience Australia, Canberra. doi:10.4225/25/53D99B6581B9A.
- 605 Zhao, Z. and M. H. Alford, 2009: New altimetric estimates of mode-1 M2 internal tides
606 in the central North Pacific Ocean. *J. Phys. Oceanogr.*, **39** (7), 1669–1684, doi:10.1175/
607 2009JPO3922.1.

₆₀₈ **List of Figures**

₆₀₉ 1 Location of TTIDE field site: a) Energy flux in a regional numerical sim-
₆₁₀ ulation. Color is the absolute value of the flux, arrows it's direction. The
₆₁₁ magenta box indicates the numerical modeling domain used in this paper. b)
₆₁₂ Detail of the bathymetry on the Tasman slope. The magenta lines indicate
₆₁₃ 100 km in the x-direction, and 300 km in the y direction in the modeling do-
₆₁₄ main used in this paper. c) The stratification used for all runs in this paper,
₆₁₅ taken from the World Ocean Atlas at 152 E, 44 S (Boyer et al. 2013). The
₆₁₆ steps are due to linear interpolation of the density between the atlas depths. 38

617 2 a) Energy flux representation of the analytical response to the forcing used
618 to drive the models used in this paper. Two mode-1 internal wave sources
619 are located to the south east (blue lines). The model domain is rotated 12
620 degrees from geographic so the shelf break approximately lies along $x = 0$.
621 The outer model domain is the rectangle with the thick green line. The
622 inner green rectangle denotes 1-km lateral resolution. Outside this rectangle
623 resolution increases 3.5% per cell to a maximum of 5-km in the second largest
624 rectangle, and outside this rectangle grid size increases to a maximum of 10
625 km. The sponge layer is indicated by the largest thin-green rectangle. The
626 250, and 3000-m isobaths are contoured, though the bathymetry is not used
627 in the analytical response. Arrows show the direction of the energy flux, and
628 are scaled by its strength. b) Energy flux of analytical response of energy
629 reflecting from a wall at $x = 0$, north of $y = 0$, in a flat-ocean domain. c)
630 Phase of reflected response.

39

631 3 a)–d) Surface x-direction velocity for four snapshots. a) is the initial condi-
632 tions (slightly modified after a tidal cycle) and d) is the steady state. Grey
633 contours are depths at 3000, 2000, 1000, and 250-m. e)–h) is depth-integrated
634 baroclinic energy flux at the same time periods, with arrows indicating direc-
635 tion.

40

636 4 Energy budget over the 19th tidal cycle of a) Barotropic to baroclinic con-
637 version; b) Baroclinic energy flux convergence ($-\nabla F_{bc}$); c) rate of change
638 of baroclinic energy; d) residual representing the dissipation in the model
639 $D = -\nabla \mathbf{F}_{bc} + \text{Conv.} - dE/dt$. The green box is the region for the energy time
640 series (figure 5b).
41

641 5 a) Integral in x to 80 km offshore of the energy terms in figure 4 for the REAL
642 case (averaged over 20th tidal cycle). Note that the barotropic-baroclinic
643 term (red) is of the same order as the baroclinic convergence (blue) and the
644 residual dissipation (gray) for most of the slope. b) Energy budget time series
645 for the “Real” case, tidally averaged, where time is normalized by $T = 12.4$
646 h, between $y = 0$ to $y = 400$ km. There is still a small residual increase in
647 the energy with time (purple), representing the accumulation of high-mode
648 energy in the region. Net barotropic-baroclinic conversion (red) is small and
649 negative, indicating a small net loss to the barotropic tide in this region. The
650 bulk of the budget is the balance between baroclinic flux convergence (blue)
651 and the residual “dissipation” (gray). c) Net flux (averaged over 20th tidal
652 cycle) in the box defined by $0 < x < 80$ km, and $0 < y < 400$ km. Green is
653 the value for the net flux (no modal decomposition). Blue bars are the modal
654 decomposition. There is a net incoming flux in mode 1 and net reflecting
655 fluxes in higher modes (primarily modes 2-4).
42

656 6 Cross sections of topographies from $y = 50$ km.
43

- 657 7 Energy flux for six geometries at tidal cycle 20. Grey depth contours are
 658 -3000, -2000, -1000 and -250 m. Arrows indicate the direction of energy flux.
 659 See figure 6 for bathymetry cross sections at $y = 50$ km. 44
- 660 8 Mode-1 decomposition of energy fluxes averaged for the 20th tidal cycle for the
 661 SHELF experiment. a) Incoming energy flux calculated from the NO TOPO
 662 simulation (figure 7a). Note that the shelf bathymetry is contoured on this
 663 plot (grey lines, and green “land”), but this bathymetry was not part of this
 664 simulation. The green line demarks the region the energy budget in the inset
 665 was integrated over. The green diamonds are the location of a synthetic
 666 mooring, and the arrow indicates the estimated incoming flux from a plane
 667 wave fit over the three moorings of the “Total” simulation (see text). b)
 668 Reflected energy flux calculated from the difference between the velocities and
 669 displacements of the Total simulation (panel d) and the “Incoming” (panel a).
 670 Blue arrow is the outgoing flux from a plane wave fit over the mooring array
 671 from the “Total” simulation. c) Energy flux cross terms between the incoming
 672 and outgoing waves. d) Total simulation from the SHELF case (figure 7d) 45
- 673 9 Energy partition as in figure 8, taking the ROUND RISE simulation as the
 674 incoming wave, and SHELF/RISE simulation as the total wavefield. 46
- 675 10 Energy partition as in figure 8, taking the RISE simulation as the incoming
 676 wave, and REAL simulation as the total wavefield. 47

677 11 a) Energy budget from 80 km by 80 km control volumes along the continental
678 slope from the 20th tidal cycle of the REAL simulations. The incoming flux
679 (red) is compared to the reflected (blue) and the cross terms (purple). b) The
680 reflection co-efficients. The blue line is R_1 , the mode-1 reflectivity in the 80-
681 km control volumes along slope from the non-linear simulation. The black line
682 is the mode-1 reflectivity from a linear model (Kelly et al. 2013a), the next
683 four grey lines are the cumulative sum of modes 2 to 5, and the last grey line
684 the sum of all the reflected energy. These do not sum up to one because the
685 linear model has some “viscosity” that removes some high-mode energy. The
686 dashed lines are the mean of R_1 from the linear model if a constant average
687 is taken (light blue, dashed), and if weighted by the diffracted beam strength
688 (purple, dashed).

48

689 12 Barotropic to baroclinic conversion averaged over the 18-th tidal period for
690 different shelf widths a) 100 km, b) 70 km, c) 40 km, and d) 20 km. Arrows
691 are barotropic flux vectors. Note how the along-slope barotropic flux is almost
692 entirely confined to conversion dipoles along slope.

49

693 13 Along-slope spectra of across slope velocity (thick lines) for the three narrow-
694 est slopes in figure 12, from velocities on the shallow shelf in these simulations.
695 The thin lines are resonance curves, formed from the cross-slope equations of
696 motion assuming harmonic motion in time and along-slope. As along-slope
697 wavenumber is varied resonant modes have a stronger response. What is
698 plotted is arbitrary units for the three slope geometries.

50

14 Terms from the energy budget for 40-km wide slope. The incoming and re-
 flected energy fluxes are computed at $x = 40$ km, and the conversion term
 integrated from the shelf to $x = 40$ km.

15 Spatial shape of modes picked out from the resonant searching technique (as
702
703 shown in figure 13) for the 70, 40 and 20-km wide slopes.

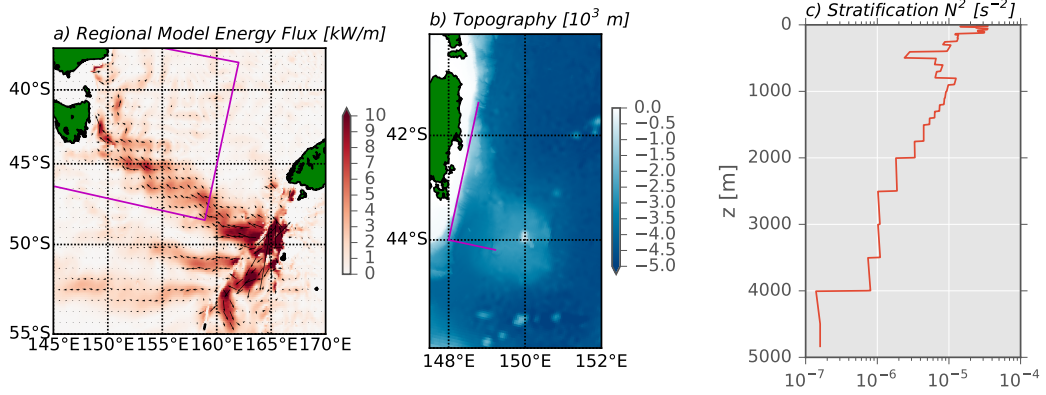


FIG. 1. Location of TTIDE field site: a) Energy flux in a regional numerical simulation. Color is the absolute value of the flux, arrows its direction. The magenta box indicates the numerical modeling domain used in this paper. b) Detail of the bathymetry on the Tasman slope. The magenta lines indicate 100 km in the x-direction, and 300 km in the y direction in the modeling domain used in this paper. c) The stratification used for all runs in this paper, taken from the World Ocean Atlas at 152 E, 44 S (Boyer et al. 2013). The steps are due to linear interpolation of the density between the atlas depths.

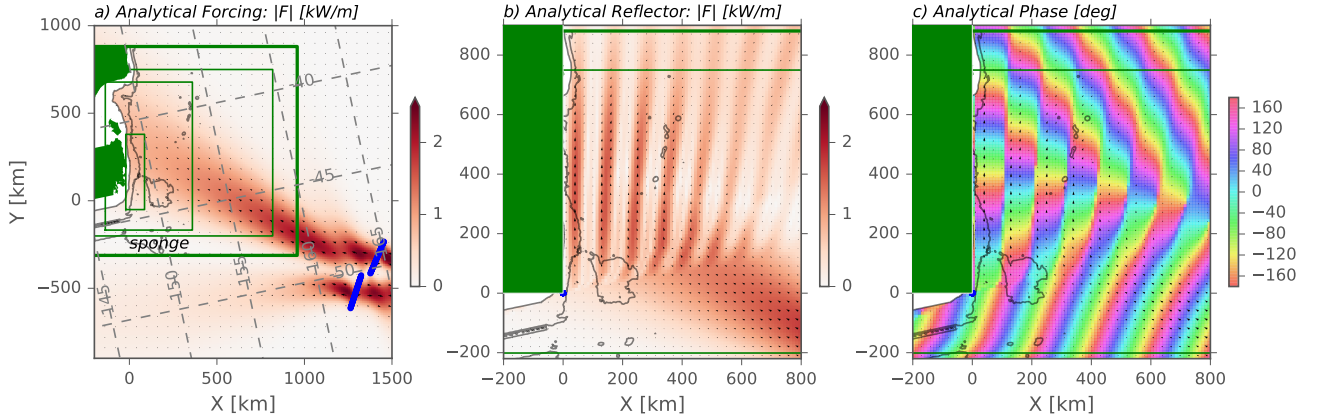


FIG. 2. a) Energy flux representation of the analytical response to the forcing used to drive the models used in this paper. Two mode-1 internal wave sources are located to the south east (blue lines). The model domain is rotated 12 degrees from geographic so the shelf break approximately lies along $x = 0$. The outer model domain is the rectangle with the thick green line. The inner green rectangle denotes 1-km lateral resolution. Outside this rectangle resolution increases 3.5% per cell to a maximum of 5-km in the second largest rectangle, and outside this rectangle grid size increases to a maximum of 10 km. The sponge layer is indicated by the largest thin-green rectangle. The 250, and 3000-m isobaths are contoured, though the bathymetry is not used in the analytical response. Arrows show the direction of the energy flux, and are scaled by its strength. b) Energy flux of analytical response of energy reflecting from a wall at $x = 0$, north of $y = 0$, in a flat-ocean domain. c) Phase of reflected response.

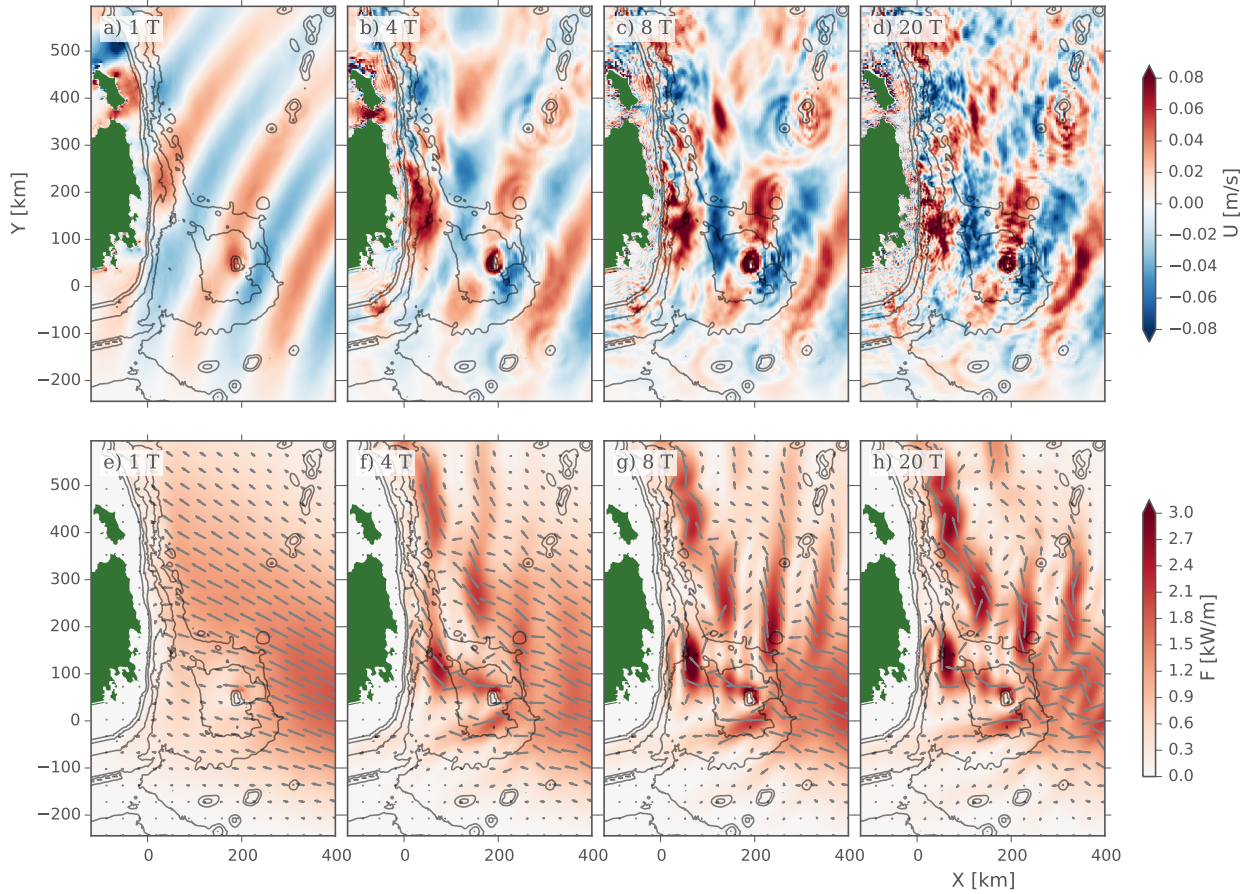


FIG. 3. a)–d) Surface x-direction velocity for four snapshots. a) is the initial conditions (slightly modified after a tidal cycle) and d) is the steady state. Grey contours are depths at 3000, 2000, 1000, and 250-m. e)–h) is depth-integrated baroclinic energy flux at the same time periods, with arrows indicating direction.

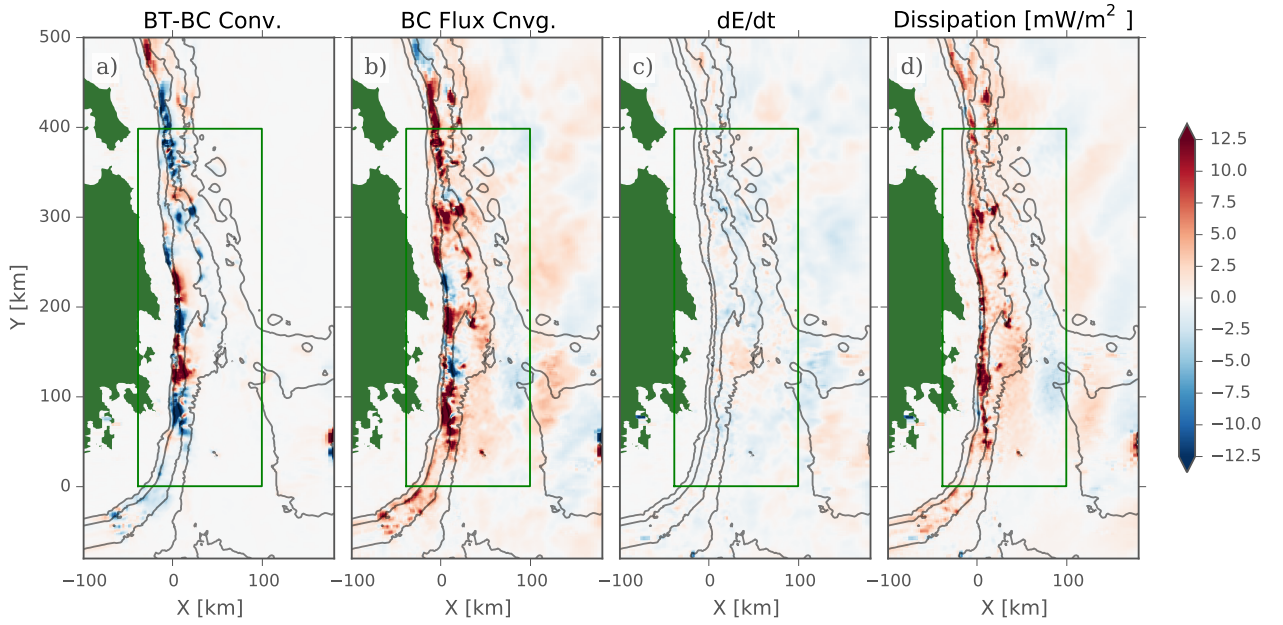


FIG. 4. Energy budget over the 19th tidal cycle of a) Barotropic to baroclinic conversion; b) Baroclinic energy flux convergence ($-\nabla F_{bc}$); c) rate of change of baroclinic energy; d) residual representing the dissipation in the model $D = -\nabla F_{bc} + \text{Conv.} - dE/dt$. The green box is the region for the energy time series (FIG. 5b).

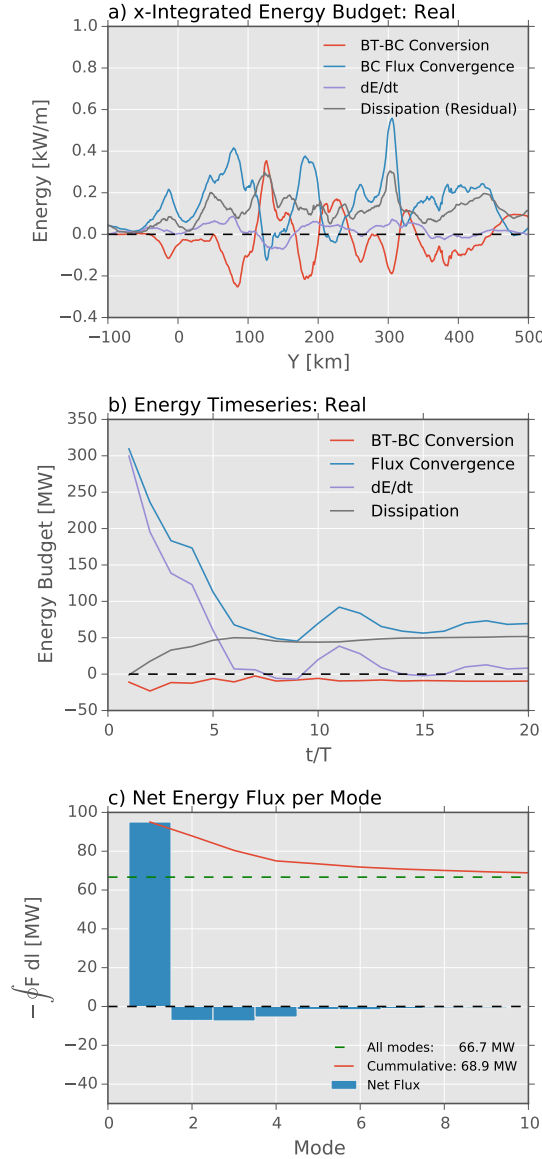


FIG. 5. a) Integral in x to 80 km offshore of the energy terms in FIG. 4 for the REAL case (averaged over 20th tidal cycle). Note that the barotropic-baroclinic term (red) is of the same order as the baroclinic convergence (blue) and the residual dissipation (gray) for most of the slope. b) Energy budget time series for the “Real” case, tidally averaged, where time is normalized by $T = 12.4$ h, between $y = 0$ to $y = 400$ km. There is still a small residual increase in the energy with time (purple), representing the accumulation of high-mode energy in the region. Net barotropic-baroclinic conversion (red) is small and negative, indicating a small net loss to the barotropic tide in this region. The bulk of the budget is the balance between baroclinic flux convergence (blue) and the residual “dissipation” (gray). c) Net flux (averaged over 20th tidal cycle) in the box defined by $0 < x < 80$ km, and $0 < y < 400$ km. Green is the value for the net flux (no modal decomposition). Blue bars are the modal decomposition. There is a net incoming flux in mode 1 and net reflecting fluxes in higher modes (primarily modes 2-4).

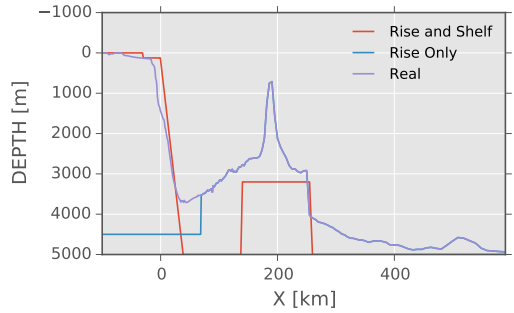


FIG. 6. Cross sections of topographies from $y = 50$ km.

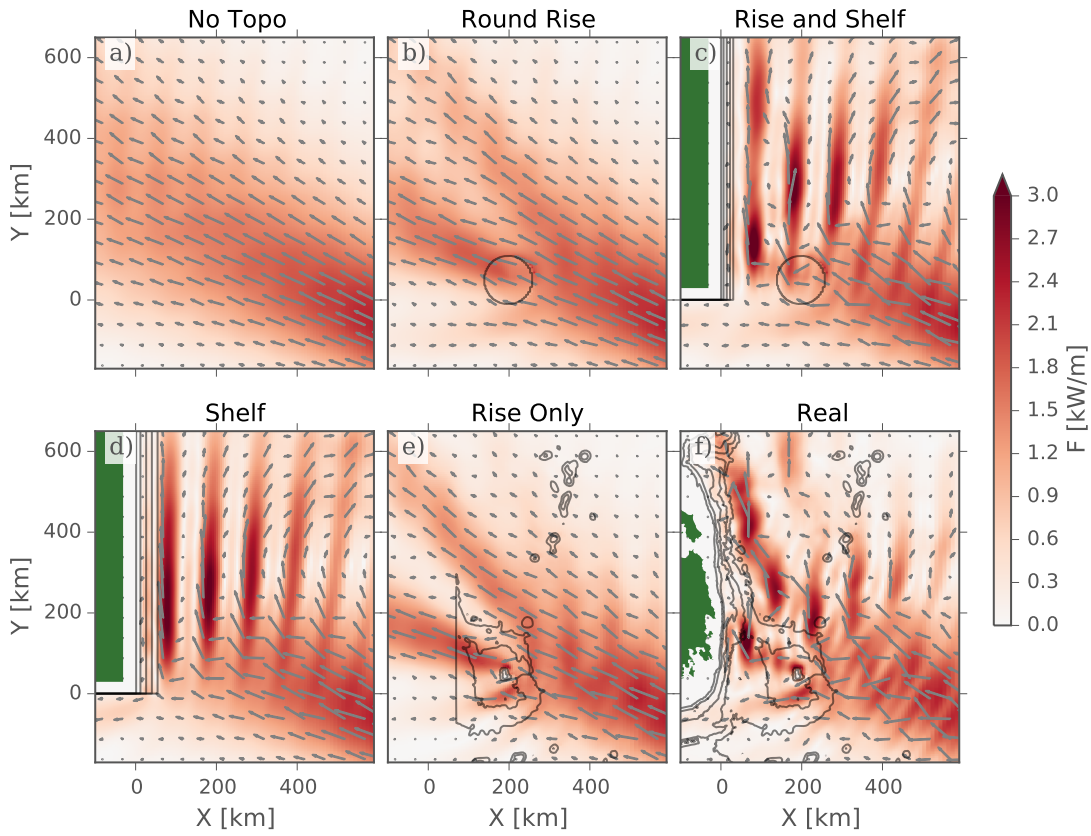


FIG. 7. Energy flux for six geometries at tidal cycle 20. Grey depth contours are -3000, -2000, -1000 and -250 m. Arrows indicate the direction of energy flux. See FIG. 6 for bathymetry cross sections at $y = 50$ km.

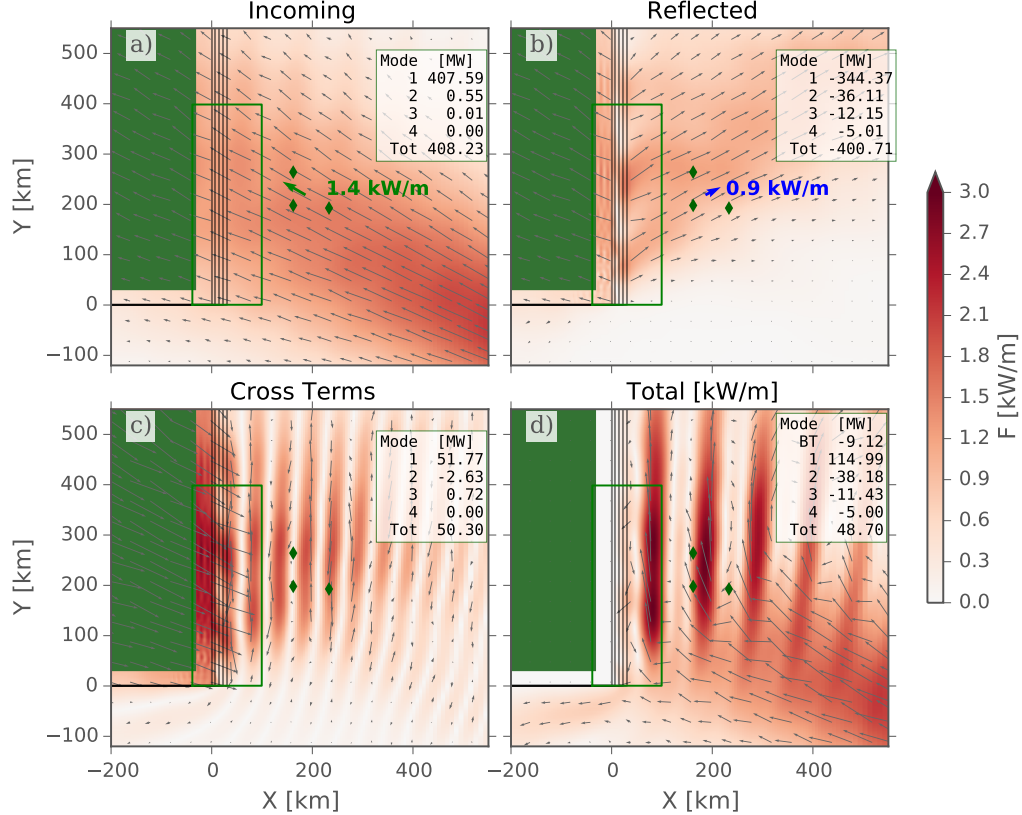


FIG. 8. Mode-1 decomposition of energy fluxes averaged for the 20th tidal cycle for the SHELF experiment. a) Incoming energy flux calculated from the NO TOPO simulation (FIG. 7a). Note that the shelf bathymetry is contoured on this plot (grey lines, and green “land”), but this bathymetry was not part of this simulation. The green line demarks the region the energy budget in the inset was integrated over. The green diamonds are the location of a synthetic mooring, and the arrow indicates the estimated incoming flux from a plane wave fit over the three moorings of the “Total” simulation (see text). b) Reflected energy flux calculated from the difference between the velocities and displacements of the Total simulation (panel d) and the “Incoming” (panel a). Blue arrow is the outgoing flux from a plane wave fit over the mooring array from the “Total” simulation. c) Energy flux cross terms between the incoming and outgoing waves. d) Total simulation from the SHELF case (FIG. 7d)

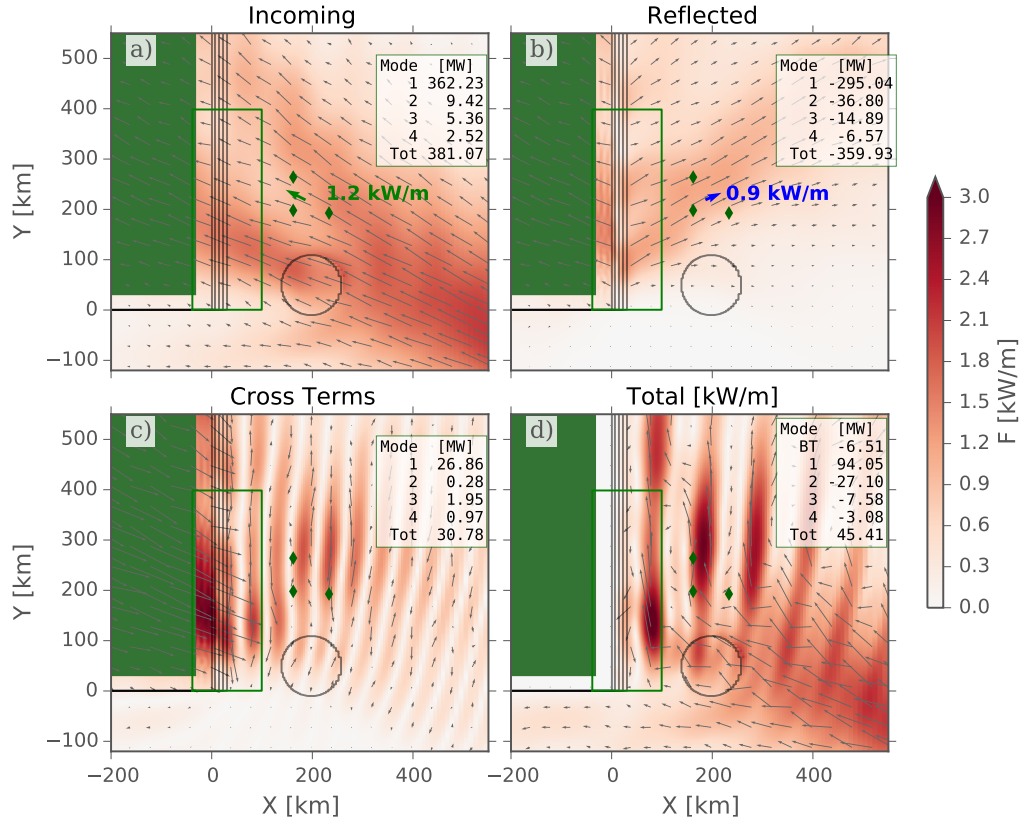


FIG. 9. Energy partition as in FIG. 8, taking the ROUND RISE simulation as the incoming wave, and SHELF/RISE simulation as the total wavefield.

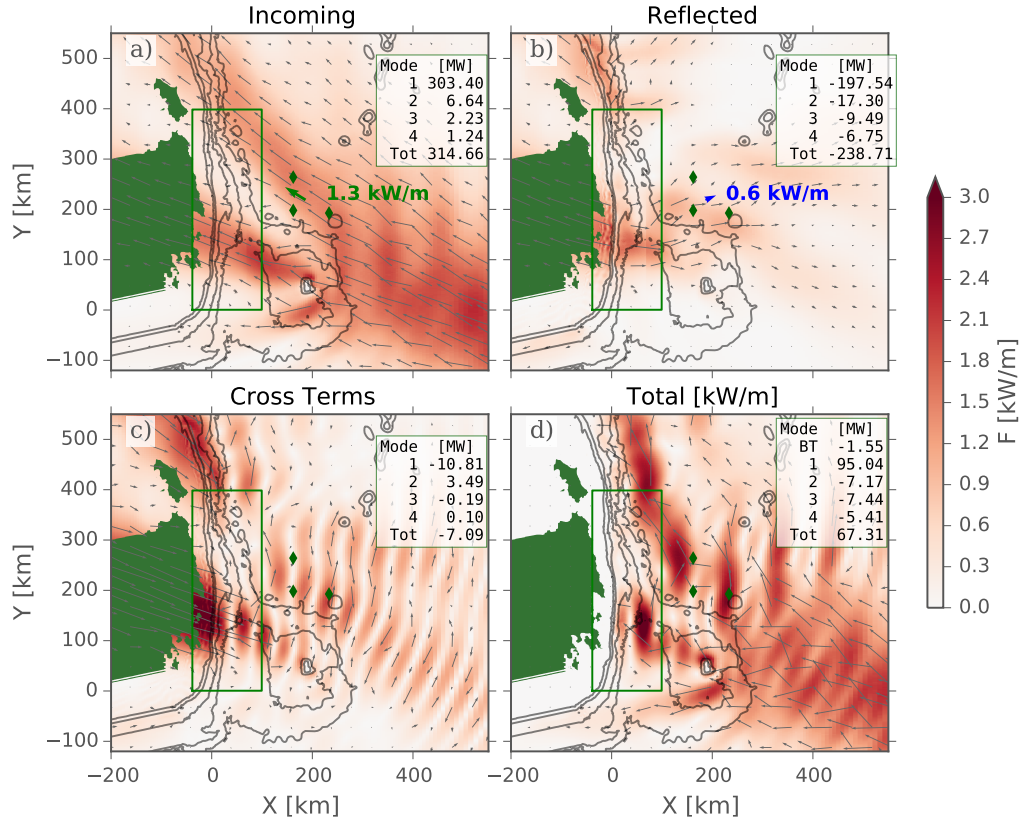


FIG. 10. Energy partition as in FIG. 8, taking the RISE simulation as the incoming wave, and REAL simulation as the total wavefield.

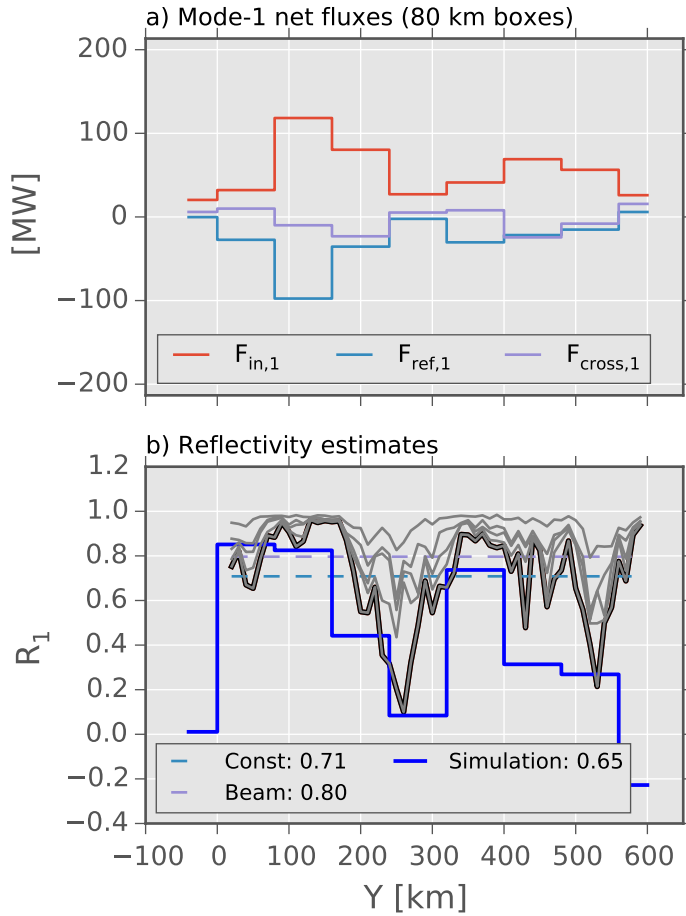


FIG. 11. a) Energy budget from 80 km by 80 km control volumes along the continental slope from the 20th tidal cycle of the REAL simulations. The incoming flux (red) is compared to the reflected (blue) and the cross terms (purple). b) The reflection co-efficients. The blue line is R_1 , the mode-1 reflectivity in the 80-km control volumes along slope from the non-linear simulation. The black line is the mode-1 reflectivity from a linear model (Kelly et al. 2013a), the next four grey lines are the cumulative sum of modes 2 to 5, and the last grey line the sum of all the reflected energy. These do not sum up to one because the linear model has some “viscosity” that removes some high-mode energy. The dashed lines are the mean of R_1 from the linear model if a constant average is taken (light blue, dashed), and if weighted by the diffracted beam strength (purple, dashed).

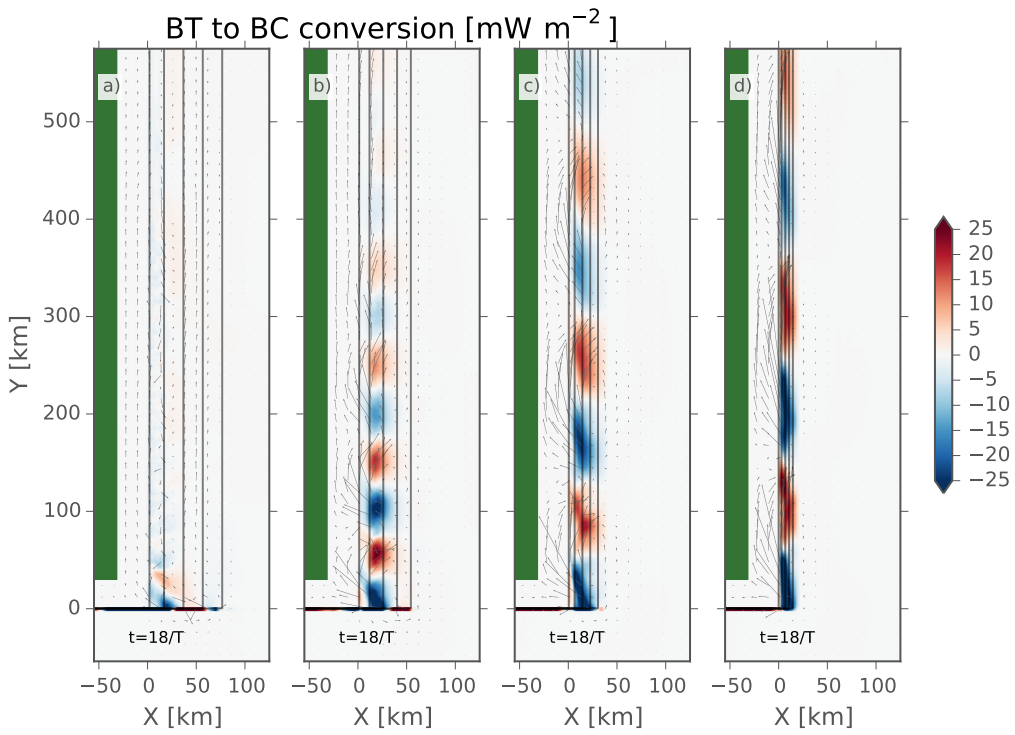


FIG. 12. Barotropic to baroclinic conversion averaged over the 18-th tidal period for different shelf widths a) 100 km, b) 70 km, c) 40 km, and d) 20 km. Arrows are barotropic flux vectors. Note how the along-slope barotropic flux is almost entirely confined to conversion dipoles along slope.

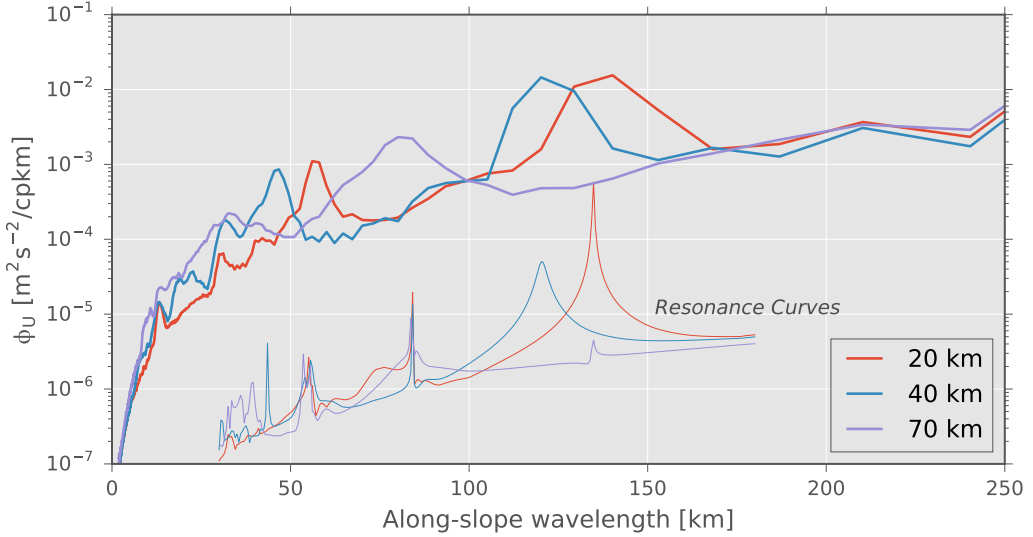


FIG. 13. Along-slope spectra of across slope velocity (thick lines) for the three narrowest slopes in FIG. 12, from velocities on the shallow shelf in these simulations. The thin lines are resonance curves, formed from the cross-slope equations of motion assuming harmonic motion in time and along-slope. As along-slope wavenumber is varied resonant modes have a stronger response. What is plotted is arbitrary units for the three slope geometries.

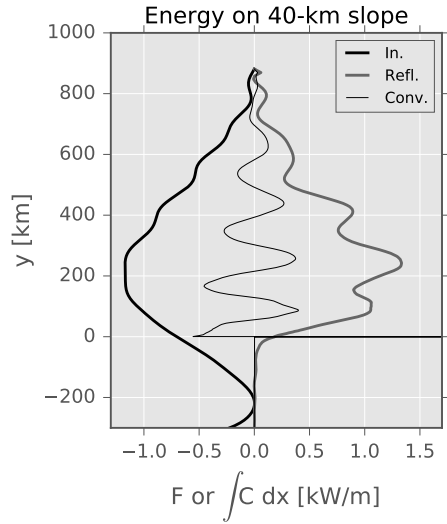


FIG. 14. Terms from the energy budget for 40-km wide slope. The incoming and reflected energy fluxes are computed at $x = 40$ km, and the conversion term integrated from the shelf to $x = 40$ km.

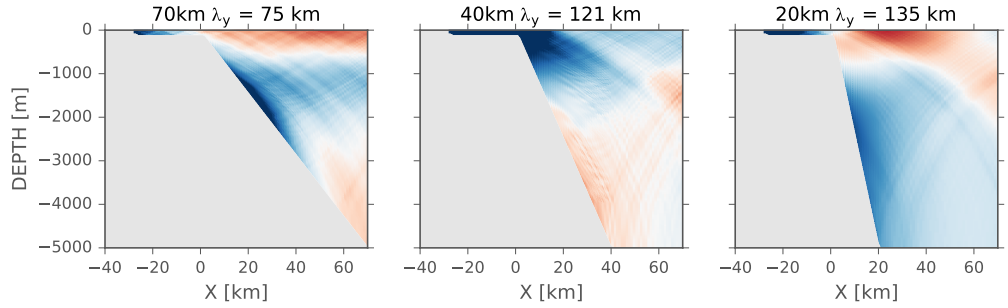


FIG. 15. Spatial shape of modes picked out from the resonant searching technique (as shown in FIG. 13) for the 70, 40 and 20-km wide slopes.